Effect of temperature on static fatigue behavior of self-healing CMC in humid air

Andre Ebel, Olivier Caty, Francis Rebillat

▶ **To cite this version:**

Andre Ebel, Olivier Caty, Francis Rebillat. Effect of temperature on static fatigue behavior of self-healing CMC in humid air. Composites Part A: Applied Science and Manufacturing, 2022, 157, 10.1016/j.compositesa.2022.106899 . hal-03955484

HAL Id: hal-03955484
https://hal.science/hal-03955484v1

Submitted on 22 Jul 2024

HAL is a multi-disciplinary open access archive for the deposit and dissemination of scientific research documents, whether they are published or not. The documents may come from teaching and research institutions in France or abroad, or from public or private research centers.

L'archive ouverte pluridisciplinaire **HAL**, est destinée au dépôt et à la diffusion de documents scientifiques de niveau recherche, publiés ou non, émanant des établissements d'enseignement et de recherche français ou étrangers, des laboratoires publics ou privés.

Distributed under a Creative Commons Attribution - NonCommercial 4.0 International License

Version of Record: https://www.sciencedirect.com/science/article/pii/S1359835X22000926
Manuscript_f5f4e3044220c85bf37df97699ebc951

Effect of temperature on static fatigue behavior of self-healing CMC in humid air.

A. Ebel[a,*], O. Caty[a], F. Rebillat[a]

[a]Univ. Bordeaux, CNRS, CEA, SAFRAN CERAMICS, LCTS, UMR 5801, F-33600 Pessac, France

*Corresponding author: ebel@lcts.u-bordeaux.fr

Abstract

Static fatigue tests at 100 MPa with unload-reload cycles were performed at 500, 550, 650 and 800°C in air + 10 %vol. H_2O on a self-healing ceramic matrix composite (SH-CMC) with a pyrocarbon interphase. The self-healing matrix was multi-layered and deposited by chemical vapor infiltration (CVI) based on the Si-B-C system. During static fatigue tests, damage was monitored during the tests with acoustic emission (AE) and electrical resistance (ER). AE demonstrated that crack initiation primarily takes place during loading for all test conditions. Evolution of ER, strain and modulus demonstrated that failure was primarily driven by interphase degradation at constant load due to unsealed cracks at temperatures below 550°C. In these conditions, crack sealing is prevented by boria volatilization and interphase degradation takes place due to both interphase oxidation and recession of the boron carbide phase surrounding the interphase.

© 2022 published by Elsevier. This manuscript is made available under the CC BY NC user license
https://creativecommons.org/licenses/by-nc/4.0/

Keywords (max. 5):

Ceramic-matrix composites (CMCs); Environmental degradation; Acoustic emission; Electrical resistivity; Fractography

Introduction

In the context of rising costs of energy and global warming, civil aviation is continuously seeking for jet engines with lower fuel consumption in order to reduce both its costs and its carbon footprint. The basic options to increase the performance of the engines are to increase the efficiency and decrease the weight of turbines. Higher efficiency require higher combustion temperatures and therefore materials with higher temperature capability. Lighter structures requires materials that have better strength and lower density [1].

Non-oxide fiber reinforced ceramic matrix composites (CMC) are attractive candidate materials for such application as they are lighter than the nickel-based superalloys traditionally used and have enhanced high-temperature capability [2]. However, these materials have limited damage tolerance and complex damage mechanisms. Therefore, the lifetime prediction methodology of components manufactured with these materials is more complex than with traditional materials such as metals.

In SiC/SiC CMCs, the high temperature performance mostly relies on the interphase's nature and its oxidation resistance over time. For CMCs with a Pyrocarbon (PyC) interphase, the presence of cracks in the matrix at high temperature can lead to a fast degradation of the mechanical properties since the interphase is consumed due to fast oxidation of carbon.

Self-healing CMCs were developed so that cracks are rapidly filled with oxide that prevent interphase oxidation. In CMCs with a pure SiC matrix, cracks can be sealed thanks to silica formation but this phenomenon is limited to temperature higher than 1000°C [3]. The use of a multilayered CVI-deposited matrix in the Si-B-C system enables crack-healing at low to intermediate temperature due to the formation of liquid borosilicate glass. This healing capability leads to longer lifetime at intermediate temperature in comparison with regular SiC/PyC/SiC composite [4]. Examples of CMCs with self-healing matrices in the Si-B-C system and SiC fibers are Cerasep A410 and A40C manufactured by Safran Ceramics.

However, the Si-B-C system has downsides in both high and low temperature range. The high temperature stability of amorphous CVI-deposited boron carbide (B_xC) is limited by its crystallization into rhombohedral boron carbide (B_4C) and the associated volume variations that may cause initiation and propagation of cracks in the matrix [5–7]. At low temperature, the healing capability of the Si-B-C system is limited by boria volatilization in humid atmosphere. Indeed, boria is known to react with water vapor to form gaseous hydroxides and oxyhydroxides. This volatilization leads to active oxidation of boron carbide [8] at temperature as low as 300°C [9]. Active oxidation of boron carbide leads to its recession. Modeling of the crack reactivity demonstrates that B_xC recession prevents any sealing [10].

SH-CMCs with open and unsealed cracks show a fast decay of mechanical properties and reduced lifetime. Early works from Moevus [11] on Cerasep A410 demonstrated that the SiBC matrix can heal cracks efficiently only above 560°C in ambient air (which typically contains around 2 vol. % H_2O). Below this

temperature, healing is not reliable and the CMC lifetime is reduced. Additional works from Momon [12] on Cerasep A410 demonstrated that lifetime decreased with temperature for a given stress in this temperature range. Works from Simon et al. [13] on Cerasep A40C at 450°C demonstrated that increasing water vapor content of the working atmosphere in this temperature range led to faster mechanical decay and decreased lifetime.

The aim of this work is to determine the effect of temperature on the crack healing capability of Cerasep A40C in humid air. In this study, static fatigue tests with unload-reload cycles were performed at 500, 550, 650 and 800°C in air + 10%vol. H_2O with acoustic emission (AE) and electrical resistance (ER) monitoring.

Materials & methods

Materials

Tests have been performed on a CMC produced by Safran Ceramics referred to as Cerasep® A40C. This material is reinforced with Nicalon^{TM} NL207 SiC fibers. There are approximately 500 fibers in each tow. Tows are woven in an interlock architecture, with 52 % of the fibers orientated in the loading direction (warp) and 48 % perpendicular (weft). A Pyrocarbon (PyC) interphase coating is deposited on the woven architecture before matrix infiltration via the Polymer Impregnation and Pyrolysis (PIP) process with pre-ceramic polymer. This PIP process is followed by chemical vapor infiltration (CVI) to deposit a thin multilayered self-healing matrix with alternating layers of SiC, B_xC and Si-B-C.

As depicted on Figure 1, the pre-ceramic resin undergoes a large thermal shrinkage during pyrolysis that results in blocks disconnected from the fibers.

These blocks are rich in Si, N, C and O and have an amorphous structure [14]. The CVI performed after PIP resulted in micrometer-thin deposits around fibers and PIP ex-polymer blocks. Boron carbide (B_xC), silicon carbide (SiC) and a mixture of SiC and B_xC (SiBC) are successively CVI-deposited. CVI-deposited SiC is highly crystallized and stoichiometric [15]. On the contrary, boron carbide is amorphous [5]. The "Si-B-C" phase is amorphous boron carbide with nano-sized crystallized SiC particles [15]. An important detail to notice on Figure 1 is that fibers are closely packed within the tows and many of them touch each other. As the CVI process is performed on the woven architecture, fibers touching each other in tows cannot be homogeneously covered by the matrix.

After machining of the densified preform to the desired shape, a second CVI deposition is performed to protect the machined surfaces. As shown on Figure 2, the resulting coating (« Seal Coat ») is much thicker and its thickness can reach several tens of microns.

The machined CMC components have open porosity of less than 10-15 vol.%. Millimeter size poresare found in between tows (macro-porosities) while micron-size porosities are observed within the densified tows (micro-porosities). With such a porosity level, the fiber volume fraction is approximately 40%.

Static fatigue tests

Tests were performed at 500, 550, 650 and 800°C. The results will be compared to the static fatigue test performed at 450°C in the same conditions by Simon et al. [13].

Specimen geometry and preparation

Tensile dog-bone specimen with 200 mm length and 4.5 mm thickness were used. The shoulders of these specimens are 24 mm wide while the reduced section is only 16 mm wide over a length of 30 mm.

Aluminum tabs were glued to the specimen's shoulders for better gripping of the sample. The glue layer between the tab and the specimen was assumed to ensure electrical isolation from the mechanical testing system.

Electrical contacts were obtained by polishing the edges at the extremities of the specimen and grinding the seal coat around the specimen shoulders 65 mm away from the specimen center. Conductive wires were connected to the specimen at the extremities and grinded areas of the shoulders with Epotek H20E silver filled epoxy resin. In this manner, the wires were in contact with the seal-coat and the bulk of the material, the inner fibers and interphase, as similarly described in [16] and [17].

Finally, a type K thermocouple was glued on the center of the reduced section with alumina paste and its alumina sleeve was glued to the side of one shoulder in between aluminum tabs.

Instrumentation

The specimens were tested with Instron 8501 electromechanical load frame using water-cooled hydraulic wedge grips, a 100 kN load cell and a 25.15 mm wide extensometer with alumina knife edges. For all tests stress was set to 100 MPa. Stress was calculated using measured specimen thickness and width in the gauge section. Unloading-reloading cycles were performed every 2h and every 24h after 24h of test. First loading and unloading-reloading cycles were

performed with a 3500 N.min^{-1} load rate. The initial modulus of the specimen is defined using the linear part of the first loading stress-strain curve. Hysteresis moduli are then computed during unloading and reloading as defined by eq. (1) and (2). For simplification purposes, only the average value of the hysteresis moduli computed during unloading and reloading will be reported.

$E_H^L = \frac{\max(\sigma^L) - \min(\sigma^L)}{\max(\varepsilon^L) - \min(\varepsilon^L)}$	(1)
$E_H^U = \frac{\max(\sigma^U) - \min(\sigma^U)}{\max(\varepsilon^U) - \min(\varepsilon^U)}$	(2)

Electrical resistance was measured using a four-point probe method in order to minimize contact resistance. The four electrical contacts are at the extremities of the specimen and on its shoulders as described in [16]. The distance between the inner electrical contacts was 130 mm. A constant direct current was applied through the outer wires whereas the associated voltage was measured between the inner wires. A 10 mA current was applied using a 6V battery for noise reduction, and a voltmeter (Agilent 34970 A) measured the induced voltage. Electrical resistance was measured using this system with a precision of 0.5 mΩ. Measurement stability was checked during 24 hours once the sample was fixed in the hydraulic jaws and heated up to the test temperature with no applied loading. The reference electrical resistance R_0 of the specimen is defined as the value measured after 24 hours stability before the first mechanical loading of the specimen. The resistance variation ΔR is then computed as defined by eq. (3) with R(t) being the resistance value measured at time t.

$\Delta R(t) = \frac{R(t) - R_0}{R_0}$	(3)

The rate of electrical resistance variation is also computed as defined by eq. (4) with dR being the variation of electrical resistance recorded during a time increment dt during the static fatigue test.

$R_{ER}(t) = \frac{dR}{dt}$	(4)

Acoustic emission signals were simultaneously recorded using a 1283 USB AE Node system equipped with a Micro30 sensor, both from Physical acoustics and Mistras. The sensor was positioned on the bottom grip as shown on Figure 3. Vacuum grease was used as a coupling agent and the sensor was held to the grip with Scotch Magic tape. Data were acquired using Mistras AEwin software at a rate of 2MHz. During acquisition, the detection threshold was set to 20 dB, the peak definition time to 50 µs, the hit definition time to 100 µs and hit lockout time to 1000 µs. Among the many descriptors of acoustic events provided by the acquisition system, only the number of events N_{AE} and the energy of each event E_{AE} will be used to compute the cumulative number of event and the cumulative energy CE_{AE} as a function of time.

For comparison purposes with acoustic measurements obtained by Simon et al. [16] on the same material using a different acquisition chain, a different sensor and a different sensor position, CE were normalized by the CE level at rupture, and the time was normalized by the failure time of the specimen.

The coefficient of emission R_{AE} defined in the literature by [12] was additionally computed. This coefficient is defined by eq. (5) with dE_{AE} being the increment of

cumulated energy recorded during an increment of time dt during the static fatigue test.

$R_{AE}(t) = \frac{dE_{AE}}{dt}$	(5)

Atmosphere

For atmosphere control, the specimens were placed in a quartz tube while gripped in the load frame. The tube had a gas inlet that enabled to maintain a gas flow with a 5 cm/s rate in the cold zone. The tube also had holes in the side so that the extensometer knifes could touch the specimen. All tests were performed in humid gas mixture with 10 vol.% H_2O, 20 %Vol. O_2 and N_2 balance at atmospheric pressure.

Heating and thermal gradients evaluation

Specimen were heated using a lamp furnace with Ushio Lighting halogen lamps and the temperature was controlled by the thermocouple fixed on the specimen. Specimen were heated to target temperature at a 20°C/min rate while force was set to 0.

As the grips of the load-frame are water-cooled, a large temperature gradient takes place in between the specimen center where the temperature is measured with the type K thermocouple and the specimen shoulders. This temperature gradient along the specimen was estimated at each working temperature in flowing humid air using a mono-chromatic pyrometer IMPAC IGA 320/23 with 2-2.5 µm spectral range mounted on a linear translation stage (see Figure 3). When the lamp furnace is operating, the reflection of the radiation from the halogen lamps on the specimen surface and the furnace walls artificially increases the temperature measured with the pyrometer. This bias

can be evaluated comparing the temperature measured with the pyrometer at the thermocouple location with the temperature measured by the thermocouple. Assuming this bias is constant all over the specimen surface, the temperatures measured with the pyrometer can be corrected.

Post-mortem characterization

Test specimen were observed by SEM after tests. For fractured specimen, fracture locations and fracture surfaces were examined. For unfractured specimen, only the specimen surface within the gauge section was examined. Specimen cross sections were prepared as well after tests using cutting with anhydrous lubricants and polishing with anhydrous polishing solutions. This procedure is required to keep borosilicate glassy phase in place.

Results

Gradients in the specimen

Static fatigue tests were performed at high temperature using cold grips. These tests cannot be interpreted correctly without considering the thermal gradient taking place in the specimen during testing. As shown on Figure 4, the temperature in the shoulders is always lower than in the gauge section and this temperature difference increases with the test temperature. The comparison of the rupture positions with the thermal gradient data shows that the final specimen failure seems to take place only in areas where the temperature is below 520°C. These areas are in the shoulders for tests performed at 650 and 550°C while it is in the reduced section for tests performed at 500 and 450°C. Theseresults are consistent with previous static fatigue test on SiBC self-

healing CMC with the same specimen geometry at 500 and 700°C in ambient air [11].

Due to these large thermal gradients, the strain measurement cannot be directly compared to the electrical resistance and acoustic emission measurements. The strain is measured on the reduced section where the temperature is the most homogeneous while the electrical resistance is measured between the shoulders, a large area where large thermal gradients are taking place. The acoustic emission sensor is placed on the bottom grip as shown on Figure 3, therefore the acoustic events taking place in the whole specimen are recorded.

Loading

The stress-strain curves during the first loading are similar whatever the test temperatures. The CMC has an elastic behavior up to 60 MPa for all test temperatures (Figure 5 A). At higher stress, the CMC starts to damage and the strain rate increases.

The Young's modulus of the undamaged CMC measured using the initial slope of strain - stress curves is in the 167-183 GPa range for all specimens. These modulus values are in the same range than ones obtained by Simon on the same material in her thesis [18]. Strain levels reached values between 0.07 and 0.09 % at 100 MPa. The two specimens that reached the largest strain levels at 100 MPa were machined from the same plate of material.

The same way as strain, electrical resistance varies also linearly with stress at the beginning of loading (see Figure 5 B). This linear behavior is linked to the undamaged CMC piezoresistance defined by eq. (6). The initial piezoresistivity

of the undamaged CMC tends to decrease as the test temperature increases. Its average value is 1.9 +/- 0.3.

$\frac{\Delta R}{R_0} = \alpha_R^{\varepsilon}\, \varepsilon$	(6)

The variation of ER with stress starts being non-linear at lower stress levels than strain, especially in the 450-500°C range. The resistance variation resulting from the first loading is between 0.2 % for test temperatures above 550°C and 0.32 % for test temperature below 500°C.

The cumulative energy (CE) of acoustics events is negligible during loading until the stress reaches 30 MPa (see Figure 5 C). For higher stress levels, CE increases exponentially with stress. The CE value reached at 100 MPa increases as the test temperature decreases.

Comparison of strain, ER and AE suggest that damage is initiated above 30 MPa but it has a measurable effect on the strain only above 60 MPa. An effect of the test temperature on damage can be derived from these measurements since strain levels, ER and CE levels reached at the end of loading for test temperature below 550°C are higher than the ones reached for test temperature above 550°C.

Static fatigue

- Mechanical behavior of the gauge section

In the reduced section of the specimens where the temperature is the most homogeneous, evolution of mechanical strain (cf. Figure 6.A) and hysteresis modulus (cf. Figure 6.B) are stabilized after a few hours at 550, 650 and 800°C. At 800°C, the strain variation due to static fatigue is so low that the strain

measurement is dominated by noise. The measured strain variations have a 24-hour period and might correspond to daily variations of the temperature in the room where the static fatigue test was performed.

However, strain and modulus can exhibit large variation at these temperatures before stabilization. These variations increase as test temperature decreases: the variations encountered at 550°C are larger than those at 800°C.

For temperature below 550°C, once the load is applied, strain does not stabilize and keeps increasing while the modulus decreases until specimen rupture. The strain and modulus variations at rupture are larger at 450°C. They are faster at 500°C and lead to a shorter lifetime. At both temperatures, the modulus measured in the last unloading-reloading cycle before failure is very close to the theoretical minimum modulus of the composite in the case of a saturation of the matrix cracking and the complete load transfer to the fibers. The minimum modulus range reported in Figure 6.B is calculated with eq. (7) from [19] using 38 vol.% for fiber fraction and values from [20] and [21] for Nicalon SiC fiber modulus.

$E_{min} = \frac{E_f V_f}{2}$	(7)

- Acoustic emission

The comparison of the CE normalized by the CE level at rupture as a function of time normalized by the failure time on Figure 7.A shows that acoustic activity takes place primarily at the beginning of the test and especially during the first loading of the specimen and the first 5 % of hold time at constant stress for all test conditions.

The evolution of the coefficient of emission R_{AE} shown on Figure 7.B demonstrates that acoustic activity decreases during the static fatigue test until the specimen fails for all test temperatures.

- Electrical resistance

Unlike acoustic activity, Figure 8.A shows that the electrical resistance of the specimen continuously rises during the static fatigue tests performed in humid air until failure except at 800°C.

At 800°C, the electrical resistance is stabilized after the first loading and its variation with time is negligible (see Figure 8.B).

At 450°C and 500°C, the rate of variation of electrical resistance initially decreases during a short time at the beginning of the test before continuously increasing until failure. At 450°C, the linearity of R_{ER} on the log scale on Figure 8.B demonstrates that the evolution of ER variation on Figure 8.A is truly exponential. At 500°C, the rate of variation reached a constant value and suggests that the electrical resistance variation is rather linear.

Tests performed in the 550-650°C range have an initially high rate that decreases with time to reach a plateau. The rate corresponding to this plateau increases as the test temperature decreases and is approximately one order of magnitude higher at 550°C than at 650°C.

Unloading-reloading cycles

Stress-strain (SS) loops measured during the unloading-reloading cycles tend to open for test temperatures below 550°C while they remain linear for higher test temperature as shown on Figure 9.

While holding at constant stress slowly affects the specimen resistance, unloading-reloading cycles can have a more dramatic effect depending on the test temperature. As shown on Figure 10, the stress-resistance (SR) curves tend to get a γ shape as the test time increases. Due to this γ shape, the resistance at the end of reloading becomes higher than the one at the beginning of unloading. This resistance variation increases with time and follows the same tendencies as the global electrical resistance variation shown on Figure 8.A.

Post-mortem observations

The specimen surfaces in the reduced section were observed after the tests. For test temperature higher than 550°C, oxide seems to flow out of cracks as shown Figure 11.

All fracture surfaces observed after testing show evidence of recession of boron carbide due to active oxidation. As shown on Figure 12, the boron carbide phase that is initially coating the fibers and the PIP SiC blocks is not observed anymore. Voids are observed instead.

The evidences of boron carbide recession along the SiC fibers in transverse crack are confirmed with cross-sectional observation perpendicular to the load below the fracture surface (see Figure 13 A). It is also observed on longitudinal cracks in fibers tows perpendicular to the load (see Figure 13 B).

Troubles were met with anhydrous cutting and polishing during the cross-section preparation and the specimen may have been exposed to water. Water may have altered oxides in the specimen such as boria. Therefore, observations made on these specimen cross-sections may not be representative of the actual oxidation of the specimen at the end of the test. In

particular, the voids observed between the fiber and the SiC phase Figure 13 could have been filled with oxide at the end of the test and react with water during cross-section preparation. However, the fact these voids are observed directly on the fracture surface on Figure 12 suggests that they were not initially filled with oxide.

On fracture surfaces, fiber pulling is limited to longitudinal tows close the specimen surface (see Figure 14 A). In tows in the middle of the specimen, fracture surfaces tend to be flat with short fiber pull-out lengths despite evidence of active oxidation of boron carbide in the external coating of the tows and around individual fibers (see Figure 14 B). A closer look at Figure 14 B also shows that fibers that touch each other fail in the same crack plane. This might be an evidence of fiber bridging.

Discussions

Damage due to loading

Comparison of the strain levels, ER and CE reached at 100 MPa on Figure 5 suggest an effect of the test temperature on the kinetics of damage during loading.

The comparison of the stress-strain curves up to 100 MPa at temperatures between 450 and 800°C from this work with the same curve obtained at room temperature from the literature [13] on Figure 15 clearly demonstrates this effect.

The most striking feature of this comparison is the ER variation. The value reached after loading up to 100 MPa at room temperature is 1.75 % while in this work, ER variation at 100 MPa does not exceed 0.25 %. Thus, the ER variation

measured at room temperature is more than 7 times higher than the ER variation measured after loading in this work.

Electrical resistance variation is associated with piezoresistivity and debonding between the matrix and the fibers assuming that the electrical resistivity of the damaged CMC around a crack is higher than in the undamaged CMC [22]. The increasing ER variation with decreasing test temperature suggest that both the crack density and/or the debonding length increase with decreasing test temperature. Another factor could be the variation of piezoresistivity with temperature.

What is more, SS and SR curves during the unloading-reloading cycle performed after loading up to 100 MPa at room temperature show respectively a slight opening and a gamma shape. In comparison, SS and SR curve during the first unload-reload cycles of the static fatigue test performed in this work and in Simon's work are essentially linear. The opening of the SS loops is proportional to the damaged length of the interface (the crack density in the matrix times the length of the debonding between the fiber and the matrix for a given crack [13]). The gamma shape of SR loops is also proportional to the interphase degradation between the fiber and the matrix. Thus, the slight opening of the SS loop and the gamma shape of the SR curve at room temperature suggest that the whole damaged length of the interphase (crack density of the matrix and the debonding length of the interphase) reached at 100 MPa at room temperature is higher than the one reached after loading at higher temperatures in this work.

Unfortunately, AE measurements performed during this tensile test at room temperature cannot be compared directly with the results of this work as they were not performed with the same setup. Nevertheless, the first acoustic events are measured around 30 MPa in all conditions. AE measurements from this work demonstrates that the CE increase faster as the test temperature decreases (see Figure 5.c). This suggest that matrix cracking during loading increases as the test temperature decreases. This would explain the increase of the strain and ER variation levels reached at 100 MPa as the test temperature decreases.

This effect of temperature on damage can be explained by residual stresses due to differences in thermal expansion coefficients between the matrix and the fiber. The self-healing matrix is obtained by a CVI process at approximately 1000°C. Due to the difference of thermal expansion coefficient between the fiber and the matrix, the matrix is under tensile load and the fibers are under compressive load at temperature below the processing temperature [23]. These stress levels increase as the temperature difference with the processing temperature increases. Therefore, the level of the tensile load in the matrix is expected to increase as the temperature decreases. As a result, the stress required to initiate cracks in the matrix is also expected to decrease as the temperature decreases.

Therefore, despite that all experiments were performed with the same initial mechanical loading (100 MPa), the resulting amount of damage in the composite might depend on the temperature. Residual stresses decrease when temperature increases, the damage due to loading increases as the temperature decreases. For a given specimen with a temperature gradient

between the reduced section and the shoulders, this effect could explain that damage remains significant in the shoulders despite the fact that stress is lower due to larger cross sectional area.

Damage during static fatigue

The evolution of CE and RAE observed in this work is very different from the one reported in the literature for static fatigue in ambient air on a similar kind of self-healing CMC [12]. For these tests, the minimum value of the coefficient of emission was reached for a duration equal to 60% of the failure time and the final failure was preceded by a large increase of acoustic activity. In this work, the coefficient of emission continuously decrease until failure and specimen failure is not preceded by any rise in acoustic activity. This latter observation suggests that the mechanism responsible for the specimen failure is not a source of acoustic events (like matrix cracking). Therefore, the crack density in the matrix can be assumed to be constant after the initial loading during whole test duration until failure.

In contrast with acoustic emission, strain, modulus and ER can have large variations during static fatigue. The extent of these variations depends on the test temperature.

For test at temperature lower than 550°C, the continuous degradation of mechanical properties and increase in electrical resistance suggest that crack healing is not taking place in the reduced section of the specimen. Consequently, the matrix and the interphase are exposed to the oxidizing gas mixture.

At 450 and 500°C, the very large electrical resistance variations at failure (200 and 100% respectively) are consistent with the very large strain variation, drop in modulus and opening of the SS loops during the unloading-reloading cycles measured in the gauge section. This confirms that damage takes place in the gauge section and suggests that the temperature is too low outside the gauge section for any thermally activated degradation mechanism to occur. This assumption is validated by the fracture location in the reduced section reported on Figure 4.

The stabilization of modulus and strain for test temperatures above 550°C suggests that cracks are healed and the interphase protected in the reduced section. This assumption is also supported by the fact that the SS curves remain closed during the unloading-reloading cycles for these test temperatures. The difference in mechanical behavior of the reduced section between tests at temperature higher than 550°C and lower than 550°C suggests that crack healing takes place at temperatures higher than 550°C. These assumptions are validated by the observation of the specimen surface in the reduced section after the tests (Figure 11).

However, due to large thermal gradients, damage still takes place in the shoulders where temperature drops below 550°C and can lead to lifetime as short as the one obtained at 500°C. The increase of electrical resistance despite the stabilization of mechanical behavior suggested that crack healing was not taking place in colder areas outside the reduced sections for tests at target temperature higher than 550°C. This assumption is confirmed by the failure location and the thermal gradient measurements reported on Figure 4. This effect of temperature on failure locations of self-healing CMC was

previously demonstrated for tests performed in ambient air in cold grips by Genet et al. [24].A striking result is that despite similar lifetimes at 500 and 550°C, resistance variations are very different. This difference of resistance variation can be linked to the extent of the most damaged zone. At 450°C and 500°C, the area where the damage leading to rupture takes place is the whole reduced section, leading to large resistance variation. At temperature above 550°C, the damage leading to rupture takes place in the shoulder in the very narrow area where the temperature and stress conditions are the most unfavorable. Due to the larger cross-sectional area in the shoulders, the local resistance is lower. Therefore, the effect of damage in this area on the global electrical resistance variation is reduced, leading to smaller resistance variations. This effect undermines the ability for electrical resistance to describe effectively the damage state of specimen with varying section.

Healing conditions

When cracks are formed at high temperature, the PyC interphase is exposed to oxidation. The consumption of PyC due to oxidation increases the debonding length between the matrix and the fiber. Within the debonding length, the stress in the fibers rises and their strain level increases. In turn, strain of the fibers drives the crack opening. For crack healing to occur, oxidation of the crack walls must produce an oxide scale that thickens faster than the crack opening rate at the beginning of the test.

The aim of the B_xC phase in the matrix is to produce fast growing liquid boria that can fill the crack very quickly at temperature above 500°C [25,26]. Unfortunately, in wet atmosphere, the reaction of boria with water produces gaseous boron (oxy-)hydroxides that lead to recession of the boron carbide

phase. This is referred to as active oxidation of boron carbide. The volatilization rate depends on both the gas velocity and the vapor pressure of boron hydroxides formed, which in turn depends on the temperature and the water vapor content in the atmosphere [27,28].

The SiBC phase in the matrix produces a borosilicate during oxidation. The formation rate of borosilicate on SiBC is lower than the one of boria on B_xC [25], the volatilization rate of borosilicate is also lower than the one of boria at a given temperature, water vapor content and gas velocity [25].

In this work, the observation of a silica-rich glassy phase flowing out of the cracks after the tests performed at temperature above 550°C supports the assumption that the crack sealing capability of the self-healing matrix in humid air relies on borosilicate formation. The formation of this borosilicate can either be the result of SiBC oxidation or the result of formation of boria from oxidation of BxC followed with dissolution of silica from enhanced oxidation of SiC in presence of boria [29,30]. However, the lack of oxide observations on the fracture surfaces where the temperature is assumed to be below 550°C demonstrates that the formation rate of the borosilicate is too low in this temperature range for the crack to heal.

What is more, the volatilization rate of the borosilicate in humid air decreases when its silica content increases [25]. The maximum amount of silica in the borosilicate at a given temperature is defined by the composition of the liquidus of the SiO_2 - B_2O_3 system and this amount increases as the temperature increases according to the silica – boria phase diagram [26]. As the maximum

silica content of the borosilicate glass remains low below 550°C, its volatilization rate remains close to the one of pure boria.

Failure mechanism

Previous works from Simon [16] on Cerasep A40C demonstrated the effect of increased water vapor content in the working atmosphere on the CMC lifetime and mechanical behavior at 450°C. Lifetime reduction and mechanical decay are faster when the water vapor content is increased. These effects were correlated with the increase of the electrical resistance of the composite. In turn, increase in electrical resistance was correlated with an accelerated degradation of the fiber interphase as electrical conductivity relies primarily on the PyC network.

The recession of the boron carbide surrounding the fibers observed on the fracture surfaces in this work can be an additional mechanism of interphase degradation. Indeed, if the boron carbide phase surrounding fibers in the tows (see Figure 1) suffers from active oxidation, the debonding length at the matrix fiber interface should increase to same extent as the boron carbide recession. Then, if the recession rate of the boron carbide is higher than the oxidation rate of PyC, it drives the interphase degradation, and thus, all the properties depending on debonding length such as strain, modulus and electrical resistance.

As boron carbide recession is also observed at 450°C, this mechanism could explain the effect of water vapor demonstrated by Simon [16]. What is more, literature on the effect of water vapor on PyC oxidation rate is scarce and the

little data available in Bertran's thesis [31] does not demonstrate any dramatic effect of water vapor.

Depending on which one is faster, both PyC oxidation and boron carbide recession can drive the decay of mechanical properties due to increasing debonding length.

The final failure of the composite is driven by fiber failure. Within the debonding length around matrix cracks, fibers are exposed to some extent to the oxidizing atmosphere. In these conditions, for a constant stress, strength of the fibers decreases with time due to sub-critical crack growth [32]. At the same time, stress in the fibers increases within the debonding length around the crack. Additionally, as the debonding length increases with time due to either PyC oxidation or B_xC recession, the length of the fibers exposed to both oxidizing atmosphere and overload increases as well with time. Therefore, the defect population exposed to overload in the fibers increases with time as well as the size of these defects. Due to the combination of these two effects, the probability that a critical defect for which the fiber strength is lower that the overload within the debonding length increases with time.

The rate of sub-critical crack growth increases with temperature [32], therefore the extent of debonding necessary to reach this probability decreases. This could explain the lower lifetime obtained at 500°C and 550°C in comparison with 450°C.

Additionally, the active oxidation of BxC in humid atmosphere around the fibers can lead to the formation of silica-rich borosilicate bridges between fibers or between fibers and the matrix that act as preferential path for crack

propagation. Such mechanism has been previously established on SiC/SiC CMCs with BN interphase exposed to humid atmosphere [28,33,34] and could be found in the present material as BxC is directly deposited on fibers after the interphase and both BxC and BN oxidize as boria.

During active oxidation of BN or BxC in humid atmosphere at a given temperature, the recession rate depends on boria volatilization rate which in turn depends on the water vapor content and gas velocity [28]. During steady-state regime of active oxidation, the oxide thickness that remains on the surface of the boron-based phase tends to a constant value X_{SS} that depends on the parabolic rate of oxide formation k_p and the linear rate of oxide volatilization k_v [35]:

$$X_{SS} = \frac{k_p}{k_v} \quad (8)$$

These two kinetic parameters might not be constant within the whole cross-section of the specimen. For instance, the boria volatilization rate k_v within the cracks is enhanced for tows close to external surface of the specimen where gas velocity on the outside surface is maximum. This would explain the large pull out length observed on longitudinal tows close to the surface which were correlated with large recession length of the B_xC around fibers. On the contrary, tows in the middle of the specimen might have limited access to water vapor and therefore low boria volatilization rate k_v. According to eq. (8), this promotes large boria scale. This boria turns into borosilicate due to boria enhanced SiC oxidation and finally to silica-rich borosilicate due to water-vapor enhanced boria volatilization [36]. Such silica-rich borosilicate might promote bridging of the fibers between each other or with the matrix.

This would explain the fact that the fracture surfaces are essentially flat beside some fiber pulling in tows close to the surface (Figure 14.a). This would also explain that the rupture is not preceded by any rise of acoustic activity (Figure 7).

Conclusions

Static fatigue tests performed in humid air in this work brings complementary knowledge with respect to the existing literature that was only focusing on the effect of temperature in dry/laboratory or on the effect of water vapor content in air at 450°C.

The combination of tests at different temperatures and measurements of thermal gradients demonstrated that Cerasep A40C was able to seal cracks formed after loading up to 100 MPa in air + 10 vol.% H_2O with 5 $cm.s^{-1}$ cold gas velocity at temperature above 550°C. The crack healing capability in these conditions relies on the formation of silica-rich borosilicate.

Below 550°C, the failure to form a crack sealant led to rising electrical resistance and decay of mechanical properties. The lack of crack sealing capability in this temperature range was related to low boria formation rate and high boria volatilization rate which prevent boria formation and lead to boron carbide recession. Boron carbide recession around the fibers has been pointed out as a new degradation mechanism for CMC with Si-B-C self-healing matrix in addition to PyC oxidation. Additionally, active oxidation of boron carbide can promote the formation of silica bridges between the surrounding fiber and matrix that strongly contribute to a strength loss of the fibers.

Author contributions

Andre Ebel: Conceptualization, Methodology, Investigation, Visualization, Writing - Original Draft; Olivier Caty: Supervision, Writing - Review & Editing; Francis Rebillat: Supervision, Writing - Review & Editing

Acknowledgements

The authors would like to thank Anne Mouret from Safran Ceramics for providing the specimens and Bruno Humez from LCTS for its expertise in mechanical testing and instrumentation.

Funding

This work was supported by the French Agence Nationale de la Recherche though the « ViSCAP » project [ANR-17-CE08-0030] (project leader: Pr. G. L. Vignoles, LCTS)

References

[1] Padture NP. Advanced structural ceramics in aerospace propulsion. Nat Mater 2016;15:804–9. https://doi.org/10.1038/nmat4687.

[2] Zok FW. Ceramic-matrix composites enable revolutionary gains in turbine engine efficiency. Am Ceram Soc Bull 2016;95:22–8.

[3] Lamouroux F, Camus G, Thébault J. Kinetics and Mechanisms of Oxidation of 2D Woven C/SiC Composites: I, Experimental Approach. J Am Ceram Soc 1994;77:2049–57. https://doi.org/10.1111/j.1151-2916.1994.tb07096.x.

[4] Bouillon E, Lamouroux F, Baroumes L, Cavalier JC, Spriet P, Habarou G. An Improved Long Life Duration CMC for Jet Aircraft Engine Applications 2002:119–25. https://doi.org/10.1115/GT2002-30625.

[5] Pallier C, Leyssale J-M, Truflandier LA, Bui AT, Weisbecker P, Gervais C, et al. Structure of an Amorphous Boron Carbide Film: An Experimental and Computational Approach. Chem Mater 2013;25:2618–29. https://doi.org/10.1021/cm400847t.

[6] Pallier C, Chollon G, Weisbecker P, Teyssandier F, Gervais C, Sirotti F. Structural changes of CVD Si–B–C coatings under thermal annealing. Surf Coat Technol 2013;215:178–85. https://doi.org/10.1016/j.surfcoat.2012.07.087.

[7] Farizy G, Chermant J-L, Sangleboeuf JC, Vicens J. SiCf–SiBC composites: microstructural investigations of the as-received material and creep tested composites under an oxidative environment. J Microsc 2003;210:176–86. https://doi.org/10.1046/j.1365-2818.2003.01128.x.

[8] Viricelle J, Goursat P, Bahloul-Hourlier D. Oxidation Behaviour of A Boron Carbide Based Material in Dry and Wet Oxygen. J Therm Anal Calorim 2000;63:507–15. https://doi.org/10.1023/A:1010133703284.

[9] Litz LM, Mercuri RA. Oxidation of Boron Carbide by Air, Water, and Air-Water Mixtures at Elevated Temperatures. J Electrochem Soc 1963;110:921–5. https://doi.org/10.1149/1.2425901.

[10] Simon C, Camus G, Bouillon F, Rebillat F. Modeling of Simultaneous Oxidation and Volatilization Phenomena Along a Crack in a Self-Healing Multi-constituent Material. Oxid Met 2017;87:381–92. https://doi.org/10.1007/s11085-016-9708-y.

[11] Moevus-Dorvaux M. Mécanismes d'endommagement, émission acoustique et durées de vie en fatigue statique du composite SiCf/[Si-B-C] aux températures intermédiaires (<800 °C). PhD Thesis. Lyon, INSA, 2007.

[12] Momon S, Moevus M, Godin N, R'Mili M, Reynaud P, Fantozzi G, et al. Acoustic emission and lifetime prediction during static fatigue tests on ceramic-matrix-composite at high temperature under air. Compos Part Appl Sci Manuf 2010;41:913–8. https://doi.org/10.1016/j.compositesa.2010.03.008.

[13] Simon C, Rebillat F, Herb V, Camus G. Monitoring damage evolution of SiC f /[Si B C] m composites using electrical resistivity: Crack density-based electromechanical modeling. Acta Mater 2017;124:579–87. https://doi.org/10.1016/j.actamat.2016.11.036.

[14] Katoh Y, Kotani M, Kishimoto H, Yang W, Kohyama A. Properties and radiation effects in high-temperature pyrolyzed PIP-SiC/SiC. J Nucl Mater 2001;289:42–7. https://doi.org/10.1016/S0022-3115(00)00681-4.

[15] Darzens S, Vicens J, Chermant JL. Microstructure and morphology of SiCf-SiBC composites. Eur Phys J - Appl Phys 2001;15:35–48. https://doi.org/10.1051/epjap:2001165.
[16] Simon C, Rebillat F, Camus G. Electrical resistivity monitoring of a SiC/[Si-B-C] composite under oxidizing environments. Acta Mater 2017;132:586–97. https://doi.org/10.1016/j.actamat.2017.04.070.
[17] Smith CE, Morscher GN, Xia Z. Electrical Resistance as a Nondestructive Evaluation Technique for SiC/SiC Ceramic Matrix Composites Under Creep-Rupture Loading. Int J Appl Ceram Technol 2011;8:298–307. https://doi.org/10.1111/j.1744-7402.2010.02587.x.
[18] Simon C. Méthodologie pour le durcissement et l'accélération d'essais sur composites à matrice céramique aéronautiques. Thèse de doctorat. Université de Bordeaux, 2017.
[19] Lamon J. A micromechanics-based approach to the mechanical behavior of brittle-matrix composites. Compos Sci Technol 2001;61:2259–72. https://doi.org/10.1016/S0266-3538(01)00120-8.
[20] Ishikawa T. Recent developments of the SiC fiber Nicalon and its composites, including properties of the SiC fiber Hi-Nicalon for ultra-high temperature. Compos Sci Technol 1994;51:135–44. https://doi.org/10.1016/0266-3538(94)90184-8.
[21] Papakonstantinou CG, Balaguru P, Lyon RE. Comparative study of high temperature composites. Compos Part B Eng 2001;32:637–49. https://doi.org/10.1016/S1359-8368(01)00042-7.
[22] Sujidkul T, Smith CE, Ma Z, Morscher GN, Xia Z. Correlating Electrical Resistance Change with Mechanical Damage in Woven SiC/SiC Composites: Experiment and Modeling. J Am Ceram Soc 2014;97:2936–42. https://doi.org/10.1111/jace.13019.
[23] Michaux A, Sauder C, Camus G, Pailler R. Young's modulus, thermal expansion coefficient and fracture behavior of selected Si–B–C based carbides in the 20–1200°C temperature range as derived from the behavior of carbon fiber reinforced microcomposites. J Eur Ceram Soc 2007;27:3551–60. https://doi.org/10.1016/j.jeurceramsoc.2006.12.006.
[24] Genet M, Marcin L, Baranger E, Cluzel C, Ladevèze P, Mouret A. Computational prediction of the lifetime of self-healing CMC structures. Compos Part Appl Sci Manuf 2012;43:294–303. https://doi.org/10.1016/j.compositesa.2011.11.004.
[25] Rebillat F, Martin X, Garitte E, Guette A. Overview on the Self-Sealing Process in the SiCF/[SI,C,B]M Composites under Wet Atmosphere at High Temperature. Des. Dev. Appl. Eng. Ceram. Compos., John Wiley & Sons, Ltd; 2010, p. 151–66. https://doi.org/10.1002/9780470909836.ch14.
[26] Rockett TJ, Foster WR. Phase Relations in the System Boron Oxide–Silica. J Am Ceram Soc 1965;48:75–80. https://doi.org/10.1111/j.1151-2916.1965.tb11803.x.
[27] Kobayashi K, Maeda K, Sano H, Uchiyama Y. Formation and oxidation resistance of the coating formed on carbon material composed of B4C-SiC powders. Carbon 1995;33:397–403. https://doi.org/10.1016/0008-6223(94)00164-U.
[28] Ogbuji LUJT. A Pervasive Mode of Oxidative Degradation in a SiC-SiC Composite. J Am Ceram Soc 1998;81:2777–84. https://doi.org/10.1111/j.1151-2916.1998.tb02696.x.

[29] Rebillat F, Garitte E, Guette A. Quantification of higher SiC fiber oxidation rates in presence of B2O3 under air. Des Dev Appl Eng Ceram Compos 2010;215:135.
[30] Opila EJ, Robinson RC, Verrilli MJ. Borosilicate Glass-Induced Fiber Degradation of SiC/BN/SiC Composites Exposed in Combustion Environments. Int J Appl Ceram Technol 2016;13:434–42. https://doi.org/10.1111/ijac.12499.
[31] Bertran X. Comportement en milieu oxydant d'un composite carbone/carbone pour applications structurales entre 150 et 400°c dans l'aéronautique civile. PhD Thesis. Université Sciences et Technologies - Bordeaux I, 2013.
[32] Ladevèze P, Genet M. A new approach to the subcritical cracking of ceramic fibers. Compos Sci Technol 2010;70:1575–83. https://doi.org/10.1016/j.compscitech.2010.04.013.
[33] Heredia FE, McNulty JC, Zok FW, Evans AG. Oxidation Embrittlement Probe for Ceramic-Matrix Composites. J Am Ceram Soc 1995;78:2097–100. https://doi.org/10.1111/j.1151-2916.1995.tb08621.x.
[34] LaRochelle KJ, Morscher GN. Tensile Stress Rupture Behavior of a Woven Ceramic Matrix Composite in Humid Environments at Intermediate Temperature — Part I. Appl Compos Mater 2006;13:147–72. https://doi.org/10.1007/s10443-006-9009-8.
[35] Tedmon CS. The effect of oxide volatilization on the oxidation kinetics of Cr and Fe-Cr alloys. J Electrochem Soc 1966;113:766–8.
[36] Jacobson NS, Morscher GN, Bryant DR, Tressler RE. High-Temperature Oxidation of Boron Nitride: II, Boron Nitride Layers in Composites. J Am Ceram Soc 1999;82:1473–82. https://doi.org/10.1111/j.1151-2916.1999.tb01944.x.

Figure captions

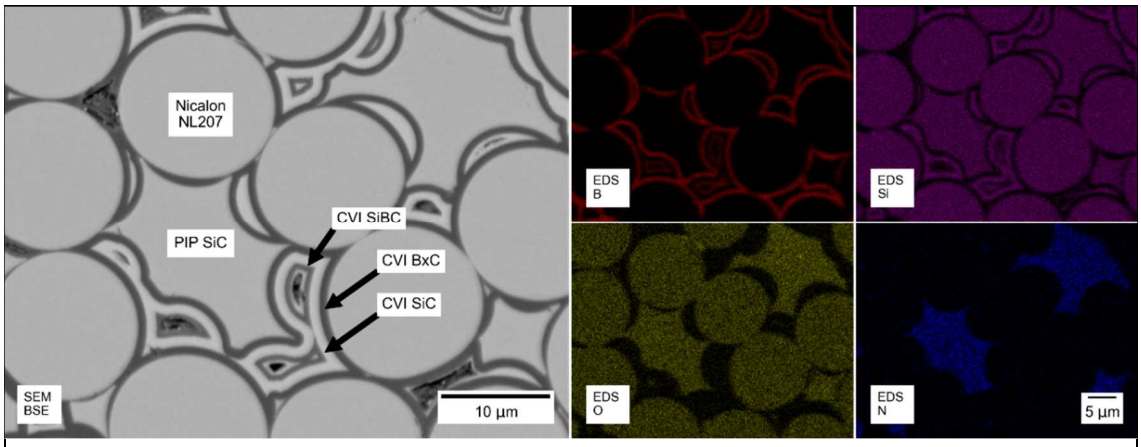

Figure 1: SEM image (left) and EDS elemental maps (right) of the Cerasep A40C microstructure at the filament scale

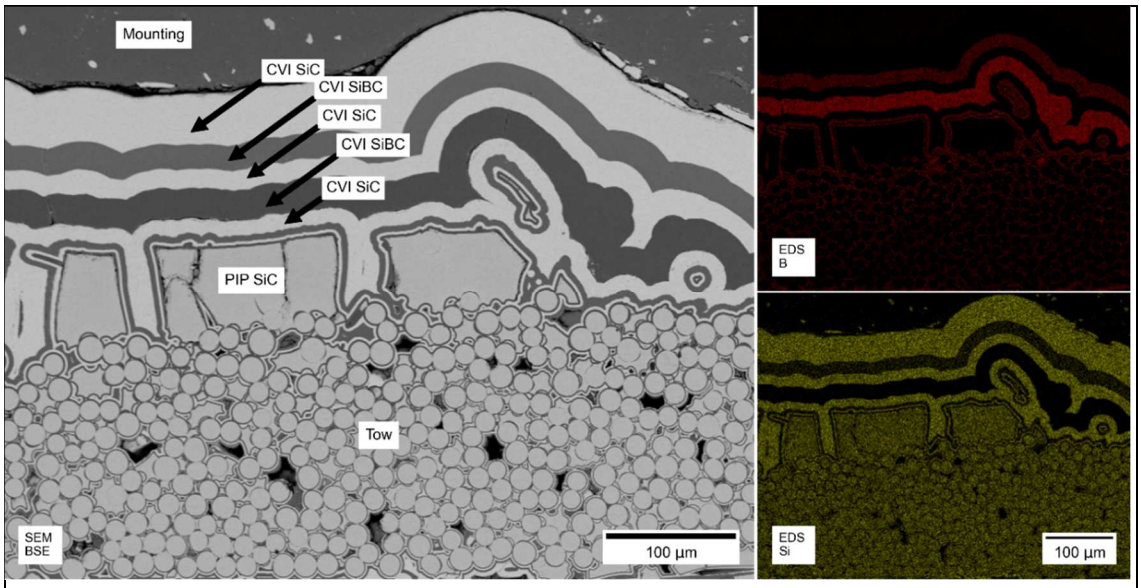

Figure 2: SEM image (left) and EDS elemental maps (right) of the Cerasep A40C microstructure at the tow scale and its seal coat

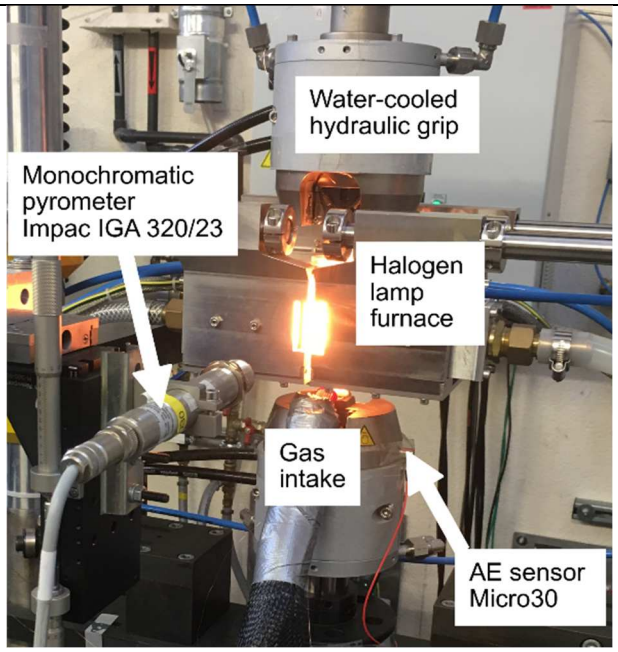

Figure 3: Picture of the thermomechanical setup during thermal gradient measurement with a monochromatic pyrometer pointed towards the sample inside the furnace

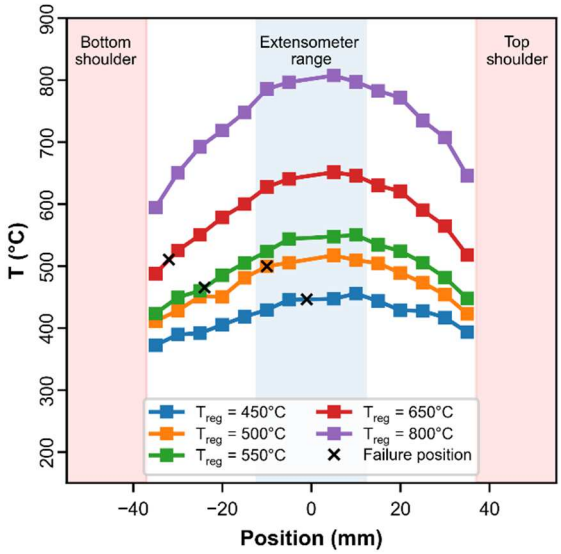

Figure 4: Thermal gradients measured at each test temperature, stress gradient due to specimen geometry and rupture location for each test condition

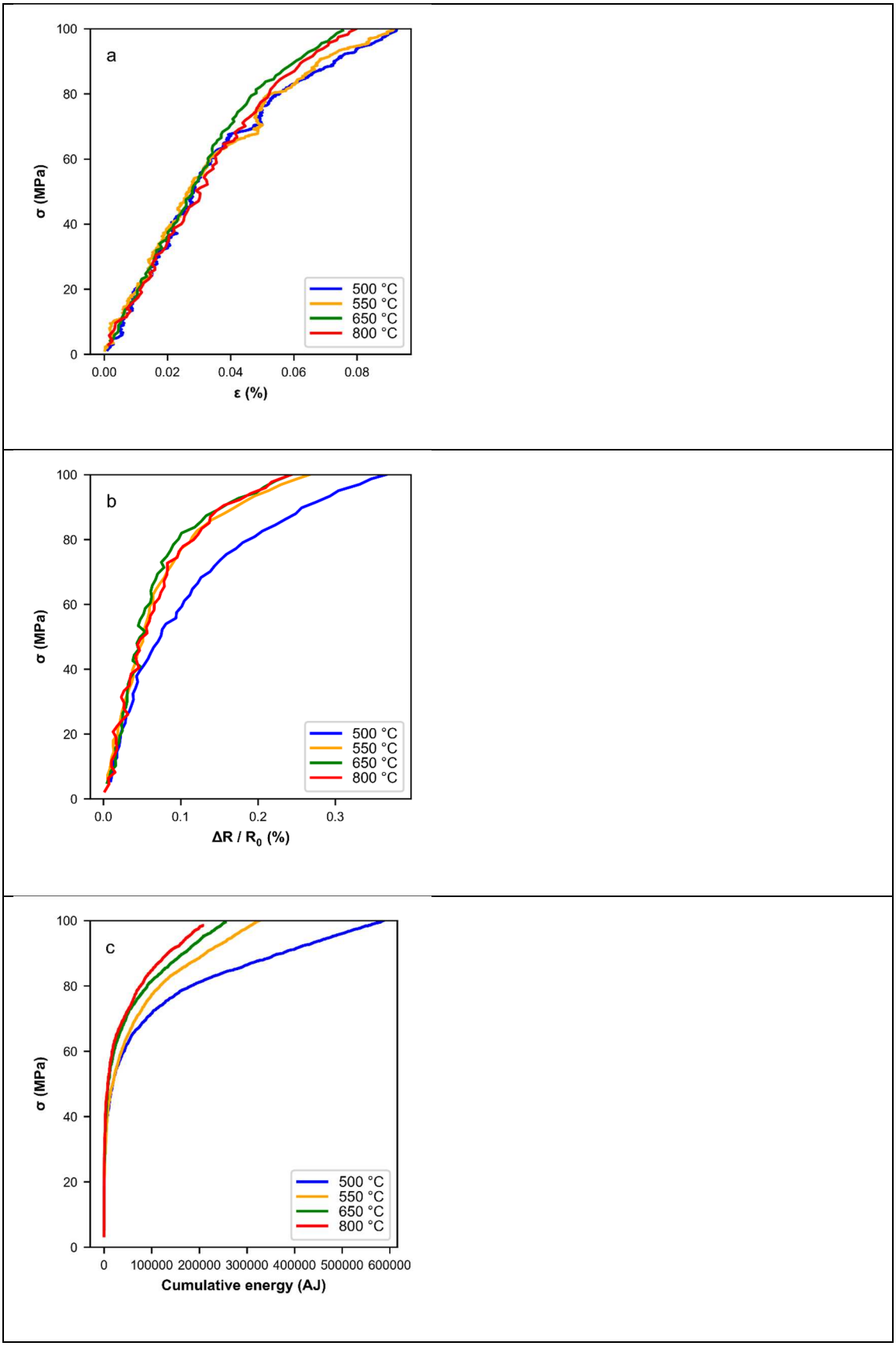
a
σ (MPa)
ε (%)
500 °C
550 °C
650 °C
800 °C
b
σ (MPa)
ΔR / R0 (%)
500 °C
550 °C
650 °C
800 °C
c
σ (MPa)
Cumulative energy (AJ)
500 °C
550 °C
650 °C
800 °C

Figure 5: Evolution of mechanical strain (a), ER variation (b) and acoustic emission (c) with stress during the first loading up to 100 MPa at 500, 550, 650 and 800°C in air + 10 vol. % H_2O.

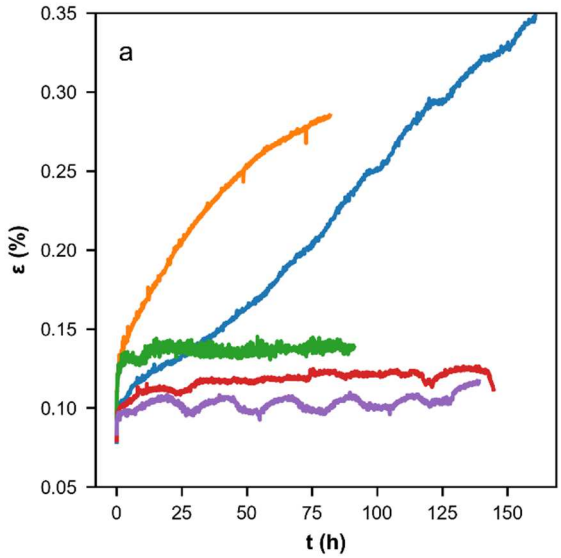

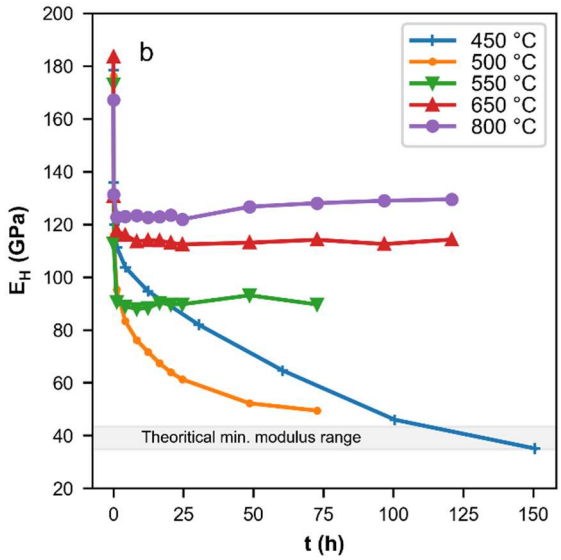

Figure 6: Evolution of mechanical strain (a), hysteresis moduli (b) with time during static fatigue tests

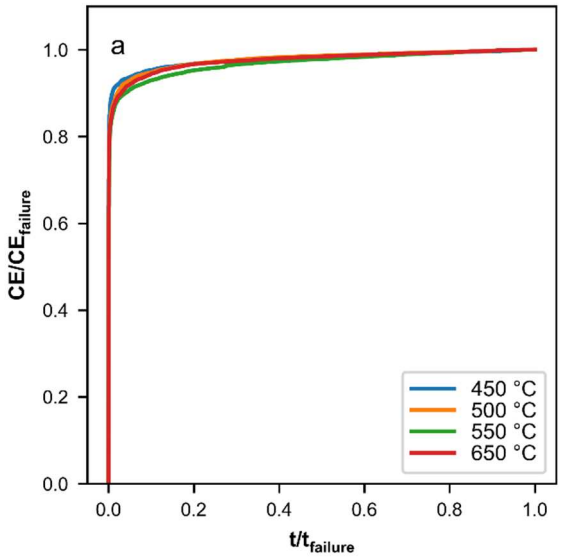

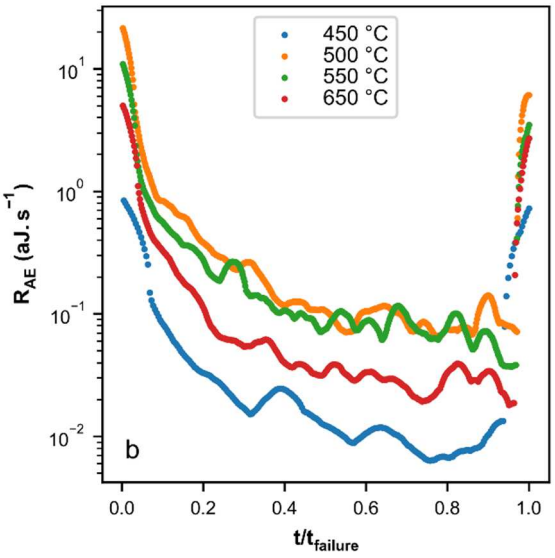

Figure 7: Evolution of the normalized cumulative energy CE (a) and the coefficient of acoustic emission R_{AE} (b) measured during static fatigue tests at 450, 500, 550, 650°C. Time is normalized with failure time for comparison purpose.

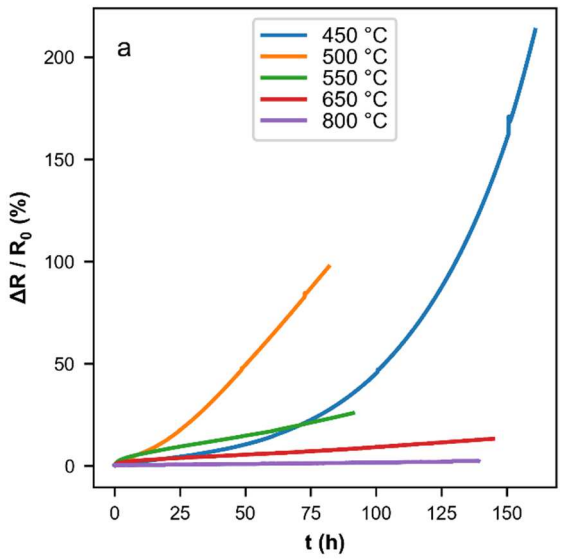

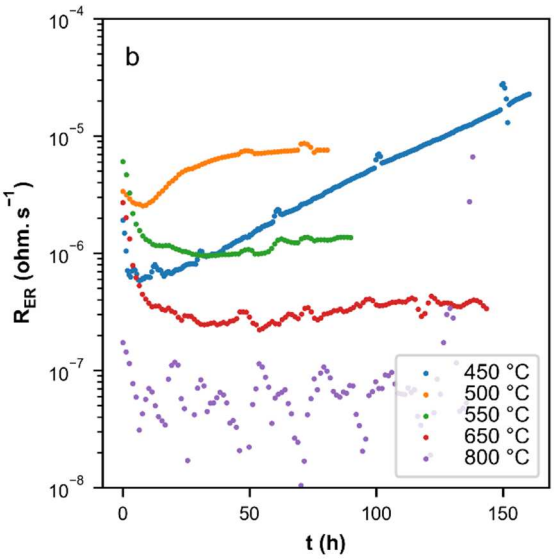

Figure 8: Evolution of the electrical resistance (a) and its variation rate (b) measured at constant load during static fatigue tests at different temperatures.

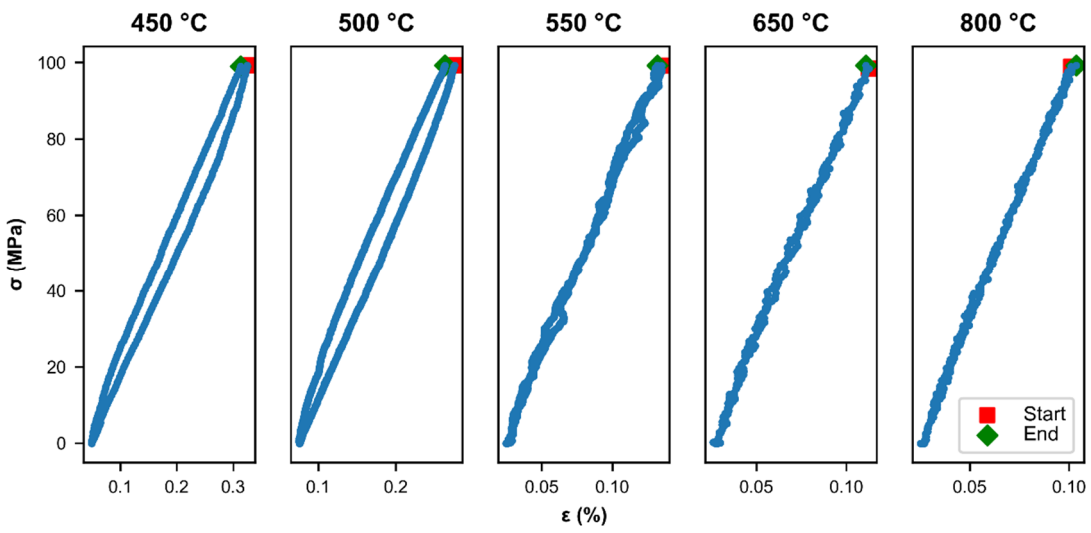

Figure 9: Mechanical stress according to the mechanical strain measured during the last unloading-reloading cycle before specimen rupture for tests at 450, 500, 550, 650°C and test ending for test at 800°C

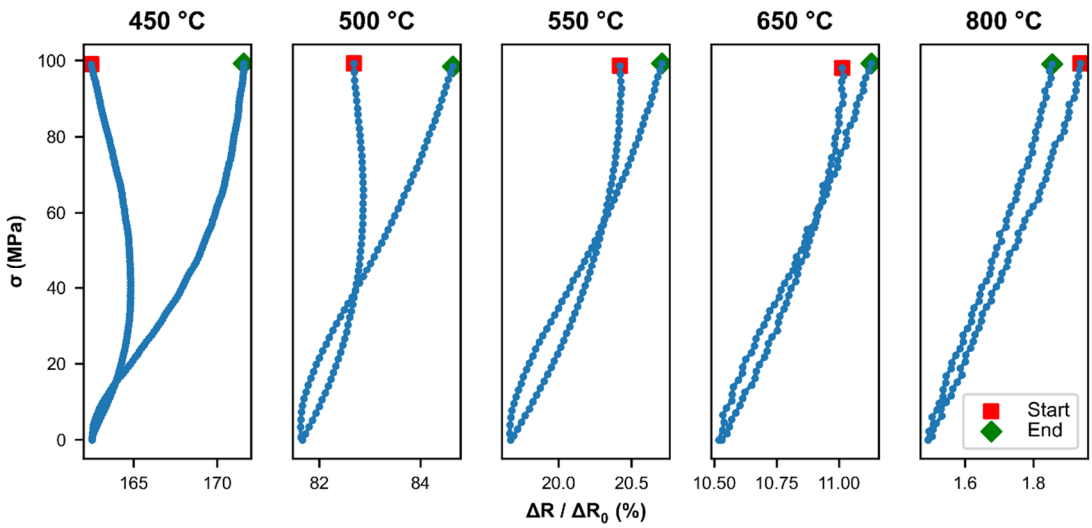

Figure 10: Mechanical stress according to the electrical resistance variation measured during the last unloading-reloading cycle before specimen rupture for tests at 450, 500, 550, 650°C and test ending for test at 800°C

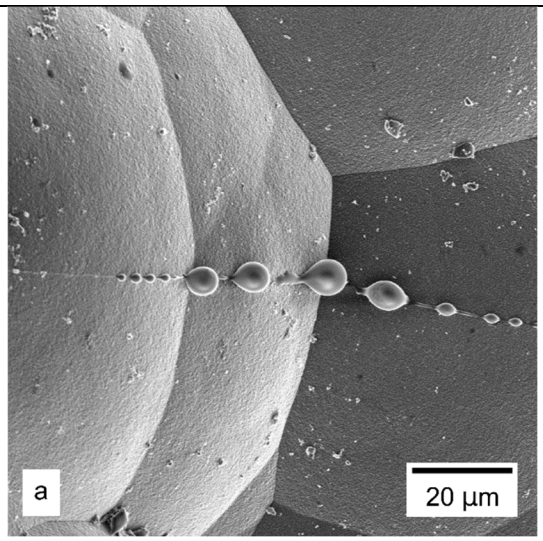

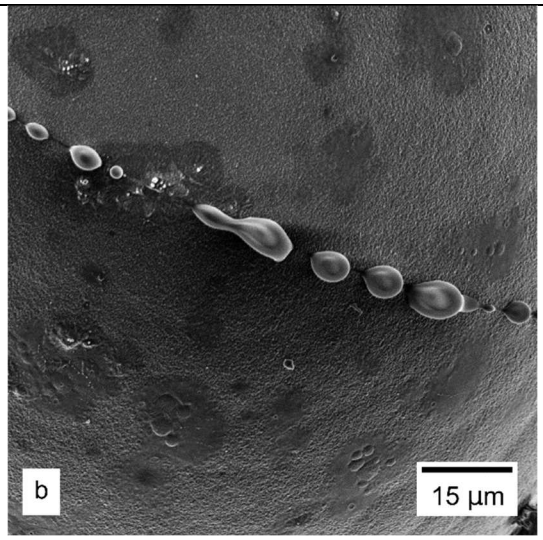

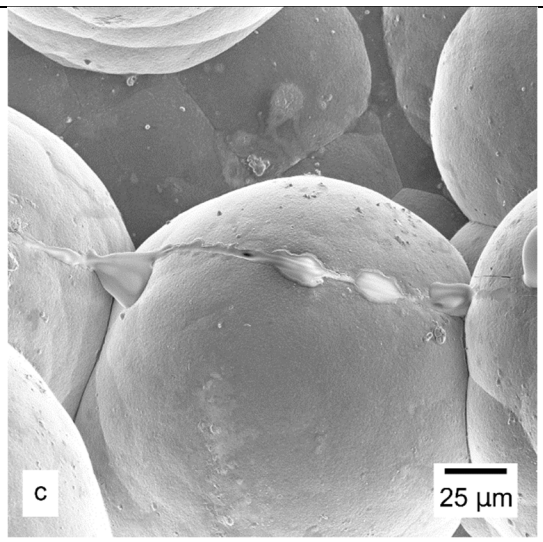

Figure 11: SEM surface observation of the reduced section after static fatigue tests at 550°C (a), 650°C (b) and 800°C (c)

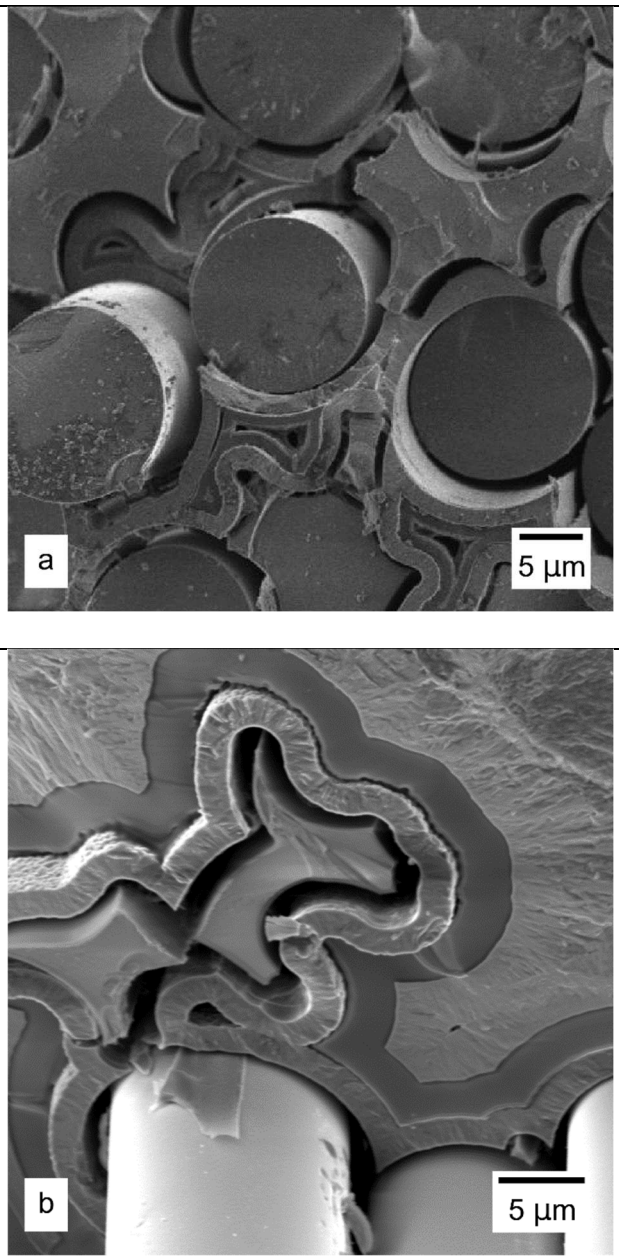

Figure 12: SEM fracture surface observation after static fatigue tests at 450°C (a) and 650°C (b)

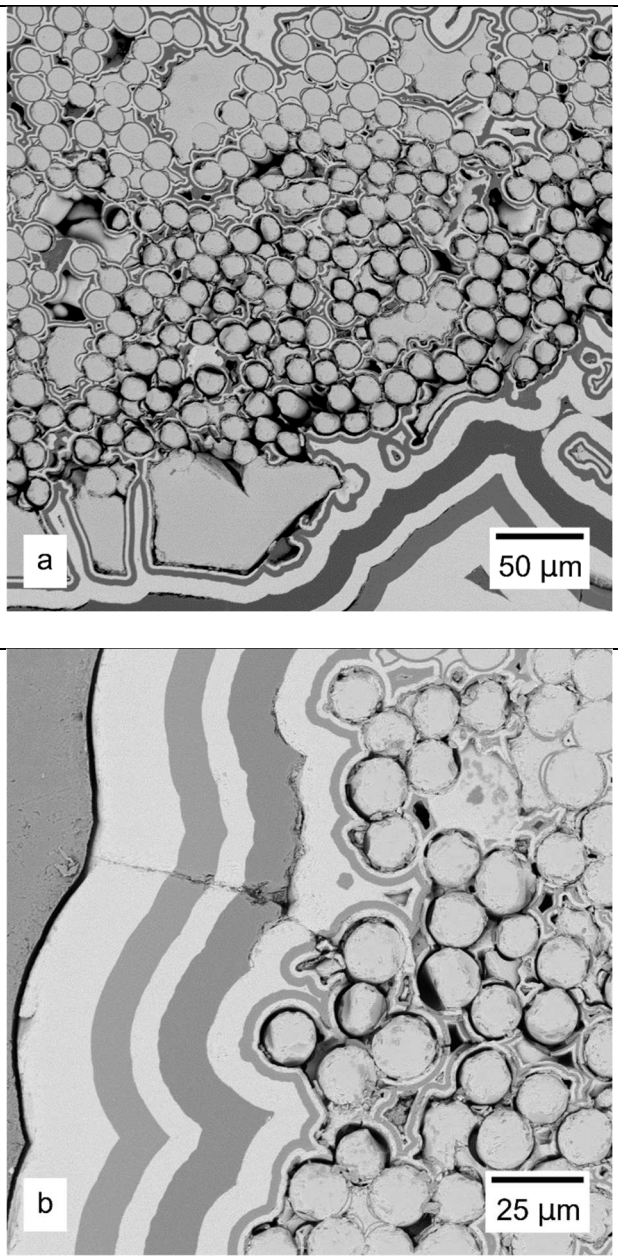

Figure 13 : SEM cross-sectional observations after static fatigue tests at 650°C: perpendicular to the load below the fracture surface (a), parallel to the load (b)

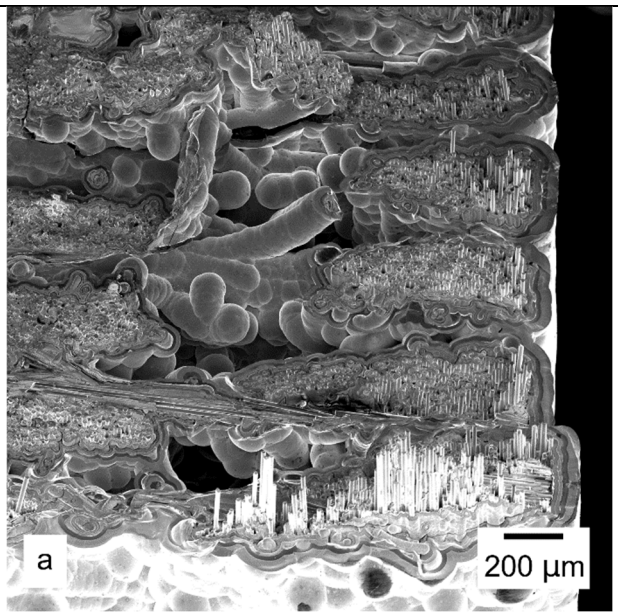

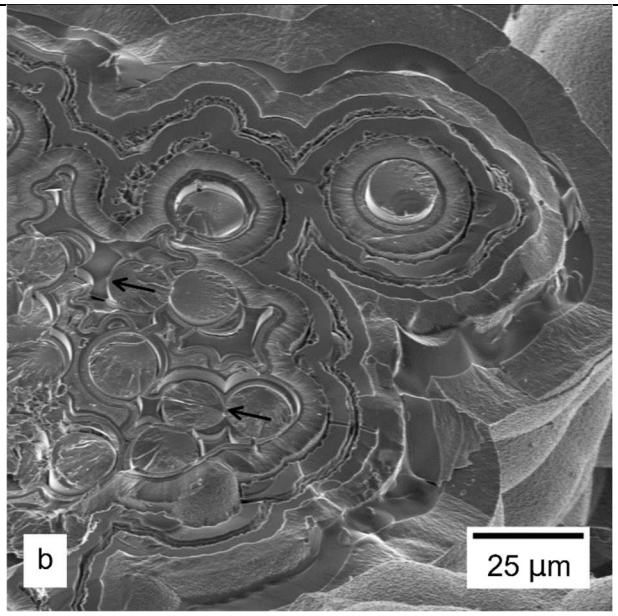

Figure 14: SEM fracture surface observation after static fatigue tests at 500°C close to the surface (a) and in the middle of the specimen with arrows indicating bridges between fibers and between fibers and matrix (b)

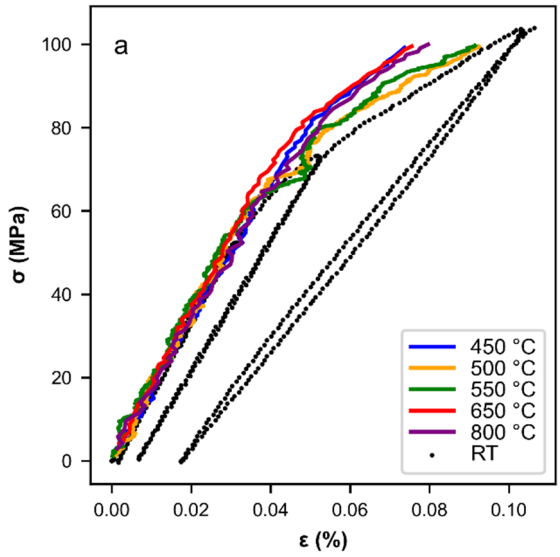

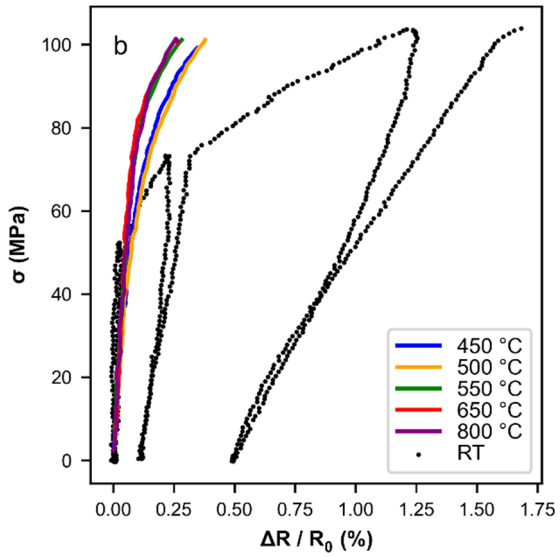

Figure 15: Comparison of the stress-strain (a) and stress-resistance (b) curve during loading up to 100 MPa in humid air at temperature between 500 and 800°C from this work, at 450 °C from [16] with data from tensile test with unloading-reloading cycles performed at room temperature on the same material [13]